

Chemical enrichment in the Ophiuchus cluster core studied by high-resolution XRISM spectroscopy

Kotaro FUKUSHIMA,^{1,*} Yutaka FUJITA,² Kosuke SATO,³ Yasushi FUKAZAWA,⁴ and Marie KONDO⁵

¹Institute of Space and Astronautical Science, JAXA, 3-1-1 Yoshinodai, Chuo-ku, Sagamihara, Kanagawa 252-5210, Japan

²Department of Physics, Tokyo Metropolitan University, 1-1 Minami-Osawa, Hachioji, Tokyo 192-0397, Japan

³Department of Astrophysics and Atmospheric Sciences, Kyoto Sangyo University, Motoyama, Kamigamo, Kita-ku, Kyoto, Kyoto 603-8555, Japan

⁴Department of Physics, Hiroshima University, 1-3-1 Kagamiyama, Higashi-Hiroshima, Hiroshima 739-8526, Japan

⁵Department of Physics, Saitama University, 255 Shimo-Okubo, Sakura-ku, Saitama, Saitama 338-8570, Japan

*E-mail: kxfukushima@gmail.com

ORCID: 0000-0001-8055-7113, 0000-0003-0058-9719, 0000-0001-5774-1633, 0000-0002-0921-8837, 0009-0005-5685-1562

Abstract

Galaxy clusters provide an ideal laboratory for investigating the chemical enrichment history of the universe because they host the hot intracluster medium (ICM), which contains various chemical elements. The X-ray observations have constituted a unique way to measure the element abundance and composition of the ICM due to their prominent emission lines in the 0.1–10 keV range. We explore the metal abundances and chemical enrichment in the cool-core galaxy cluster, Ophiuchus, by using a 217 ks XRISM data set. The abundances of Si, S, Ar, Ca, Cr, Mn, Fe, and Ni are accurately determined using high-resolution spectroscopy. We find that the average uncertainties of chemical composition, which are reported as X/Fe ratios, are only 10–20%. The X/Fe abundance pattern of the Ophiuchus centre is remarkably consistent with solar, which is reminiscent of the Hitomi constraint on the Perseus core. The observed abundance pattern can be replicated globally by linear combination models of core-collapse, including massive progenitors, and Type Ia supernovae. While nucleosynthesis models typically underestimate the Ca/Fe ratio, a substantial contribution of Ca-rich gap transients may help improve the deficit of Ca. High-resolution spectroscopic data can enable us to estimate the underlying impact on the chemical enrichment from subclasses of Type Ia supernovae.

Keywords: astrochemistry — nuclear reactions, nucleosynthesis, abundances — galaxies: abundances — galaxies: clusters: intracluster medium — galaxies: clusters: individual: Ophiuchus — X-rays: galaxies: clusters

1 Introduction

Supernova (SN) explosions play a crucial role in the synthesis and ejection of metals in the universe. Generally, core-collapse SNe (CCSNe) produce light α -elements of O, Ne, and Mg (e.g., Nomoto et al. 2013), and Type Ia SNe (SNe Ia) dominate the forge of the Fe-peak elements (Cr, Mn, Fe, and Ni; Seitenzahl et al. 2013). A significant fraction of these elements now resides within the intracluster medium (ICM) that permeates the entire volume of galaxy clusters. Thus, measuring the metal abundances in the hot gas in galaxy clusters gives us a unique understanding of the evolution of chemical enrichment on the most enormous scale in the universe.

The elemental abundances in the ICM have been well investigated using X-ray spectroscopic data because prominent emission lines of metals are present in the 1–10 keV band (Mernier et al. 2018a; Sanders 2023, for recent reviews). Thanks to the fleet of modern X-ray observatories (Chandra, XMM-Newton, Suzaku, and Hitomi), we have made considerable progress in studies on the cosmic abundances for O, Ne, Mg, Si, S, Ar, Ca, Fe, and Ni, especially around the brightest cluster galaxies (BCGs). These metals are considered primary products of SNe in the BCG. We can also test the model calculations of the SN nucleosynthesis by comparing them with the observed abundance pattern (e.g., Sato et al. 2007; Mernier et al. 2016). In particular, the Hitomi observation

of the Perseus cluster revealed that the pattern of abundance ratio to Fe (X/Fe) in the ICM is entirely consistent with our solar (Simionescu et al. 2019). Hence, whatever the meaning of this agreement with the solar composition, constructing a chemical enrichment model that can explain the abundance pattern measured by X-ray observations will directly provide a key to unravelling the chemical enrichment history of our local environment.

The recent X-ray observatory XRISM has been in operation since 2023 (Tashiro et al. 2025), installing the X-ray telescope with a micro-calorimeter instrument offering a high-energy resolution of about 5 eV in the 1.7–12 keV band (Resolve, Ishisaki et al. 2025; Kelley et al. 2025). As for now, XRISM has demonstrated its great suitability for measuring the bulk and turbulent velocities of the ICM (e.g., Rose et al. 2025; XRISM Collaboration et al. 2025a, 2025c, 2025d, 2025b). In addition, the non-dispersive high-resolution spectra provided by calorimetric spectroscopy are also a valuable asset for abundance measurements in the ICM (Hitomi Collaboration et al. 2017; Simionescu et al. 2019). Therefore, our next leap will be achieved by XRISM.

In this sense, the Ophiuchus cluster (redshift = 0.00296, Durret et al. 2015) is an excellent target as the second X-ray-brightest cluster to Perseus. Despite the presence of a cool core, Ophiuchus hosts a relatively high-temperature ICM, $kT \sim 7$ –9 keV at the innermost region (Fujita et al. 2008), resulting in a simple spectrum dominated by Fe He α and Ly α lines. This advantage enables us to

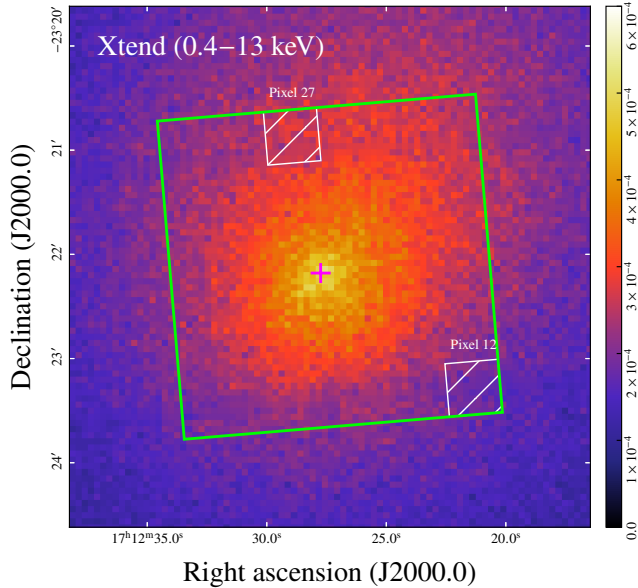


Fig. 1. Xtend exposure-corrected image in the 0.4–13 keV band of the Ophiuchus cluster. Colour bar indicates the flux in units of counts s^{-1} . The larger square indicates the Resolve FoV. The white-hatched ones represent the excluded pixel channels, 12 and 27. The cross marks the position of the BCG.

easily model the ICM emission compared to typical cool-core systems, such as Centaurus, considerably contaminated by Fe XXIV or XXIII lines. The Fe abundance at a central 100 kpc region is moderate about 0.6 solar (Fujita et al. 2008; Million et al. 2010; Werner et al. 2016; Gatuzz et al. 2023). Gatuzz et al. (2023) has also reported that the Si, S, Ar, and Ca abundances can be constrained using the stacked XMM-Newton data while only the upper limit has been obtained for Ni.

In this paper, we will analyse the Resolve data of the central region of the Ophiuchus galaxy cluster. We focused on the abundances of Si, S, Ar, Ca, Fe, and Ni throughout the entire core. Recent SN nucleosynthesis yields from some literature are examined to reproduce the observed abundances obtained with Resolve. This paper is structured as follows. In Section 2, we summarise our XRISM observation and data reduction. In Section 3, details of our spectral analysis are demonstrated. We interpret and discuss the results in Section 4. In this work, we adopt the cosmological parameters of $H_0 = 70 \text{ km s}^{-1} \text{ Mpc}^{-1}$, $\Omega_m = 0.3$, and $\Omega_\Lambda = 0.7$. All abundances are expressed relative to the proto-solar values from Lodders et al. (2009). The statistical errors are given at the 1σ confidence level unless stated otherwise.

2 Observation and Data reduction

The central region of the Ophiuchus cluster was observed by XRISM from March 31 to April 6, 2025 (OBSID = 201006010), aiming to (R.A., delc.) = $(258.^\circ 115, -23.^\circ 369)$. Figure 1 shows the X-ray image of the Ophiuchus centre observed by the X-ray CCD array onboard XRISM (Xtend, Noda et al. 2025; Uchida et al. 2025). In this work, we only use the data from Resolve, a microcalorimeter instrument covering a $3.1 \times 3.1 \text{ arcmin}^2$ field of view (FoV) with 36 pixels (Ishisaki et al. 2025; Kelley et al. 2025). In the closed gate valve configuration, the sensitive energy

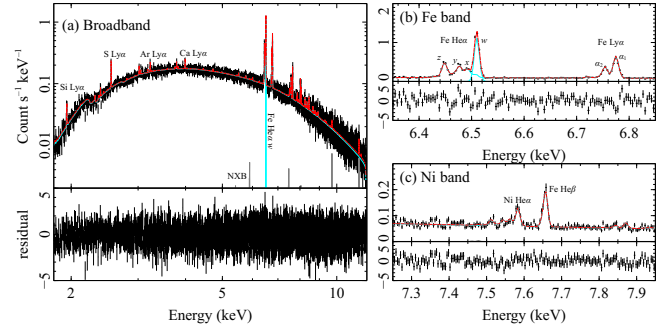


Fig. 2. (a) Broadband Resolve spectrum of the Ophiuchus centre. The best-fitting model is shown by a red dashed line, which comprises an ICM component with a Gaussian for the Fe $\text{He}\alpha-w$ line shown by cyan solid lines. A thin grey line indicates the NXB component. Residuals in terms of $(\text{data} - \text{model})/\sqrt{\text{model}}$ are also shown. (b, c) Zoom-up views around Fe and Ni lines. The prominent metal emission lines we focus on in this work are marked in each panel.

band of Resolve spans about 1.7–12 keV. The Resolve data were processed with the latest version 3 pipeline software (PROCVER = 03.00.013.010) and analysed using XRISM FTOOLS wrapped in HEASoft version 6.35 and calibration database version 11 (XRISM CALDB; gen20241115 and rs120250315). Following the standard screening procedures described in the XRISM Data Reduction Guide ¹, we extracted high-resolution events from the entire array shown in figure 1, which constructs a spectrum with an energy resolution of 5 eV at 6 keV averaged over FoV. The cleaned exposure time of the Resolve event is 217 ks after the screening. We generated a response matrix using the rslrmf task with size = X ² and simulated an effective area with the xrtraytrace and xaxmaarfgen procedures. We excluded pixel channels 12 and 27 from this work following the prescription of Fujita et al. (2025).

3 Analysis and Results

3.1 Spectral fitting

Here, we analyse X-ray spectra extracted from the FoV of Resolve. We use XSPEC package version 12.15.0 (Arnaud 1996) and the latest ATOMDB version 3.1.3 to produce a collisional ionisation equilibrium (CIE) plasma. The non-X-ray background (NXB) contribution to the Resolve spectrum (XRISM Collaboration et al. 2024) is taken into account by including the model components with a power law and multiple Gaussians for instrumental lines ³, in our spectral fitting, rather than subtracting that. The spectrum is rebinned to have a minimum of 1 count per energy bin, and we fit it using the C-statistics (Cash 1979), to estimate parameters and their errors without bias (Kaastra 2017). Figure 2(a) shows the broadband spectrum of the ICM in the Ophiuchus core. Prominent Ly α emission lines from Si, S, Ar, Ca, and Fe are detected. Additionally, there are He α lines of Fe and Ni; in particular, Ni He α is separated from the Fe Ly β line (figures 2(b) and 2(c)), both of which have been thoroughly blended in ICM spectra by CCD (e.g., de Plaa 2013; Fukushima et al. 2022).

¹ https://heasarc.gsfc.nasa.gov/docs/xrism/analysis/abc_guide/xrism_abc.html

² With this option, the Gaussian core, the exponential tail, the escape peaks, the Si K α emission line, and the electron loss continuum are taken into account for a line spread function.

³ https://heasarc.gsfc.nasa.gov/docs/xrism/analysis/nxb/nxb_spectral_models.html

Table 1. The best-fitting spectral parameters of the Ophiuchus centre for each modelling.

	1T	2T		DEM*		
		temperature			—	
kT_1	7.21 ± 0.06	11.0 ± 0.6			—	
kT_2	—	4.5 ± 0.2			—	
kT_{mean}	—	—			7.2 ± 0.3 (7.22 ± 0.19)	
σ_{kT}	—	—			5.1 ± 0.8 (4.8 ± 0.6)	
		metal content			—	
	global	local	global	local	global	local
Fe	0.537 ± 0.008	0.521 ± 0.011	0.623 ± 0.016	0.59 ± 0.04	0.611 ± 0.017 (0.617 ± 0.013)	0.602 ± 0.013 (0.622 ± 0.018)
Si/Fe	1.4 ± 0.3	1.3 ± 0.3	0.97 ± 0.19	1.0 ± 0.2	0.81 ± 0.16 (0.82 ± 0.17)	0.84 ± 0.17 (0.82 ± 0.17)
S/Fe	1.83 ± 0.15	1.74 ± 0.16	1.30 ± 0.11	1.14 ± 0.18	1.21 ± 0.10 (1.21 ± 0.10)	1.17 ± 0.10 (1.15 ± 0.10)
Ar/Fe	1.22 ± 0.19	1.20 ± 0.19	0.90 ± 0.18	0.90 ± 0.18	0.91 ± 0.14 (0.91 ± 0.14)	0.94 ± 0.15 (0.90 ± 0.14)
Ca/Fe	1.32 ± 0.16	1.36 ± 0.18	1.06 ± 0.12	1.3 ± 0.3	1.13 ± 0.13 (1.11 ± 0.13)	1.13 ± 0.15 (1.09 ± 0.15)
Cr/Fe	1.3 ± 0.4	1.4 ± 0.4	1.1 ± 0.3	1.4 ± 0.5	1.3 ± 0.3 (1.2 ± 0.3)	1.2 ± 0.4 (1.2 ± 0.4)
Mn/Fe	0.9 ± 0.4	0.8 ± 0.5	1.1 ± 0.4	0.9 ± 0.5	1.2 ± 0.5 (1.1 ± 0.4)	0.9 ± 0.5 (0.8 ± 0.5)
Ni/Fe	1.33 ± 0.11	1.36 ± 0.13	1.34 ± 0.12	1.39 ± 0.18	1.33 ± 0.12 (1.31 ± 0.11)	1.33 ± 0.14 (1.28 ± 0.13)
	statistics			—		
C-statistic/dof	18259/18547		18181/18544		18193/18546 (18190/18544)	

* Fitting results without the Fe $\text{He}\alpha-w$ line are provided in parentheses.

To reproduce the ICM emission, we use the CIE model modified by a Galactic extinction presented as $\text{phabs} \times \text{CIE}$. The absorption column density N_{H} is fixed at 3.34×10^{21} (Willingale et al. 2013), which includes both H I and H₂ effects considering the low Galactic latitude ($b \sim 9^\circ$). The photoelectric absorption cross sections are retrieved from Verner et al. (1996). Note that N_{H} is unimportant in our energy band as the absorption with only H I (HI4PI Collaboration et al. 2016) provides consistent results. Since the ICM emission is very bright at the entire FoV, we do not include any astrophysical emission from the front or backside of the ICM. For example, we estimate the cosmic X-ray background (CXB) contribution that can affect the temperature estimation in the Resolve band. The brightness of the CXB emission is well established as $S_{\text{CXB}} \sim 11 \text{ cm}^{-2} \text{ s}^{-1} \text{ sr}^{-1} \text{ keV}^{-1}$ at 1 keV (Cappelluti et al. 2017). While we include an absorbed powerlaw component with $\Gamma = 1.45$ with this brightness, its flux accounts for only 0.92% of that of the ICM component in the 2–10 keV range. The AGN activity of this cluster is also negligible (e.g., Fujita et al. 2025).

3.2 Metal abundances

First, we test the isothermal CIE modelling, denoted as the 1T model, where $\text{CIE} = \text{bvvapec}$. We let the ICM temperature (kT), turbulence velocity, redshift, and the Si, S, Ar, Ca, Cr, Mn, Fe, and Ni abundances free to vary. The abundances of elements lighter than O are set to 1 solar, and those of metals from O to Al are linked to Fe⁴. The abundances of the other elements with atomic numbers lying between the species above are linked to those of the nearest lower-number elements (e.g., Ti = Ca). We also perform local or narrowband fits within the energy bands around the most prominent lines of each element, excluding faint Si. The obtained kT and elemental abundances are shown in table 1. The metal content of the ICM from 1T is uniformly larger than unity. One caveat is that the isothermal assumption of the multiphase ICM could lead to an underestimation of the Fe abundance (e.g., Gastaldello et al. 2021). As described in Fujita et al. (2025), the ICM of the

Ophiuchus centre exhibits at least a biphasic state.

Next, we assume a multiphase ICM temperature structure with $\text{CIE} = \text{bvvapec} + \text{bvvapec}$ called the 2T model and $\text{CIE} = \text{bvvgadem}$ referred to as the differential emission measure (DEM) model. The metal content and the line-of-sight bulk velocity are shared between the two components in the 2T model, and the velocity dispersions are calculated separately. As summarised in table 1, these models result in a higher Fe abundance than that of 1T; thus, the X/Fe ratios are closer to the solar values. Both global and local abundances are consistent with each other and those from the 2T model, maintaining the solar composition of the ICM of the Ophiuchus core. Although both 2T and DEM improve the fit statistics, the statistical errors of abundance measurements are smaller with DEM than with 2T, especially for the local Ca/Fe estimate. This schism would be due to the coupling of the intensities of the two components and their abundance, with the reproduction of the Ca line being about evenly contributed by both. Therefore, we prefer the abundances from DEM with reasonable multi-temperature modelling.

Finally, we remove the Fe $\text{He}\alpha-w$ line from the ATOMDB code and add a Gaussian to model this line as $\text{CIE} = \text{bvvgadem} + \text{gauss}$. This prescription is used to account for resonance scattering in the central region that reduces the Fe $\text{He}\alpha-w$ line intensity (e.g., Hitomi Collaboration et al. 2018). We employed this method only in the DEM model. As discussed in Fujita et al. (2025), the optical depth of the w line at the very core of Ophiuchus can reach about 1, possibly leading to resonance-scattering effects. Indeed, the w/z ratio measured by Gaussians is 15% lower than the CIE prediction. The derived abundances are given in parentheses in the DEM column of table 1, which are globally consistent with the original modelling and the solar abundance ratios. Afterwards, we use these values as benchmarks for this work. In this benchmark result, our detection of Cr and Mn in the Ophiuchus core is at the 3.3σ and 1.7σ significance, respectively, with respect to the zero metallicity. Modelling uncertainties of abundance measurements are provided as 1σ deviations for each trial with 2T and DEM: $\sigma_{\text{Si/Fe}} = 0.09$, $\sigma_{\text{S/Fe}} = 0.06$, $\sigma_{\text{Ar/Fe}} = 0.014$, $\sigma_{\text{Ca/Fe}} = 0.08$, $\sigma_{\text{Cr/Fe}} = 0.08$, $\sigma_{\text{Mn/Fe}} = 0.16$, $\sigma_{\text{Ni/Fe}} = 0.04$. The differences be-

⁴ Note that these species do not make prominent line signals in the 1.8–12 keV band.

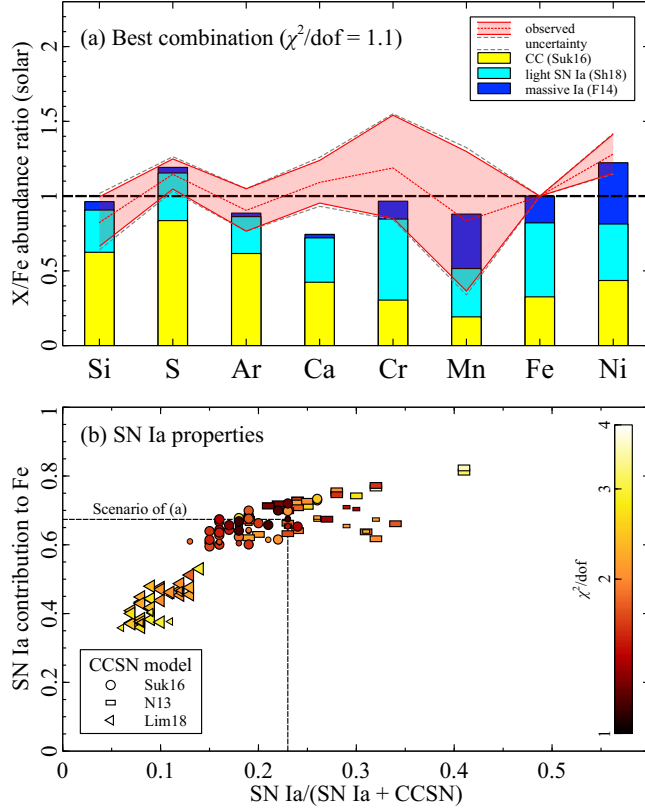


Fig. 3. (a) Observed relative abundance patterns obtained from FoV and the best-fitting result of SN nucleosynthesis models comprising Suk16, F14, and Sh18. The shaded area represents the observed pattern with statistical errors, and the dashed lines limit their total 1 σ confidence levels that are calculated by summing the statistical and modelling uncertainties (see Section 3.2) in quadrature. The histogram shows contributions to abundance ratios from each SN type. (b) SN Ia contribution plotted against its number fraction to total SNe. Colour scale indicates the χ^2/dof values for each combination. The best-fitting model demonstrated in (a) is marked by dashed lines. The small markers show the models, including pure-deflagration options (see table 2).

tween ATOMDB v3.1.3 and SPEXACT v3.08.02 (Kaastra et al. 1996, 2025) are only up to 2% in abundance ratios, which is small compared to the modelling biases of up to 11%.

4 Discussion

4.1 Solar chemical composition of the Ophiuchus core
 The Fe abundance about 0.6 solar at the Ophiuchus centre ($\lesssim 100$ kpc) is consistent with the Suzaku result of Fujita et al. (2008), and possibly those of Chandra and XMM-Newton (Million et al. 2010; Werner et al. 2016; Liu et al. 2019; Gatuzz et al. 2023), except for their proposed abrupt peak and/or depletion at the very core ($\lesssim 20$ kpc). Then, we show the X/Fe abundance pattern relative to the proto-solar value in the ICM of the Ophiuchus core (figure 3(a)). The abundance ratios are remarkably consistent with the solar value while the Ni/Fe ratio is relatively high at about 1.3 solar, which is the first robust constraint of Ni abundance in Ophiuchus. Recently, Gatuzz et al. (2023) reported that the Si/Fe, S/Fe, Ar/Fe, and Ca/Fe values are close to solar ratios within the 100 kpc central region of Ophiuchus, which is entirely consistent with our results.

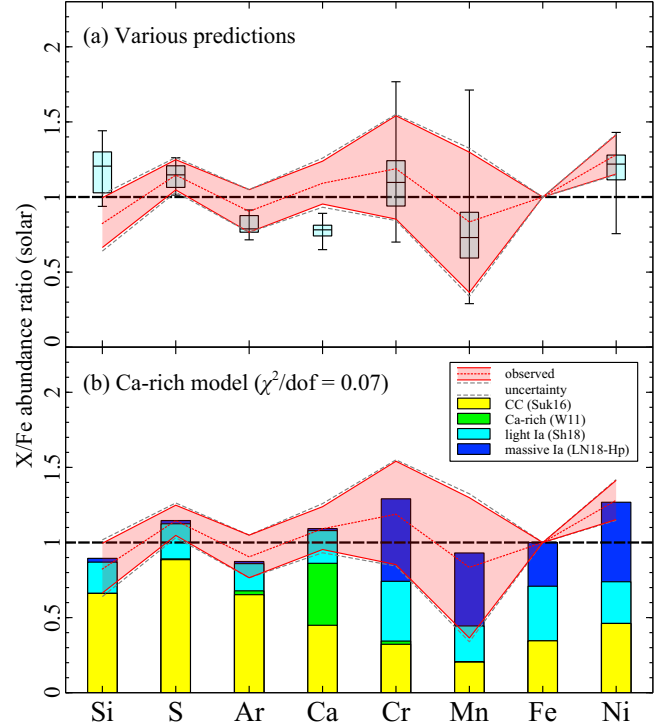


Fig. 4. (a) Abundance patterns predicted by 126 combinations of SN yields compared to the observed values. Crosses are predicted abundances from each combination model, and their medians, 1/4, and 3/4-quadrants are given by boxes. Bars show the max-min intervals of each expected value. (b) The same as figure 3(a), but the yield of Ca-rich transient is added (Waldman et al. 2011, W11).

Given that the absolute abundance of Fe is subsolar, the metallicity and composition of the Ophiuchus core are similar to those of Perseus (Hitomi Collaboration et al. 2017; Simionescu et al. 2019). Mernier et al. (2018a) and Simionescu et al. (2019) discussed in detail the implications of the observed solar composition in the ICM. Unless the elemental abundances are effectively *frozen out* to around the solar value after star formation at redshift = 2–3, irrespective of subsequent enrichment processes, a plausible interpretation is as follows: the super-solar ratios of Si/Fe, S/Fe, Ar/Fe, and Ca/Fe by early CCSN enrichment diminished over time as a substantial quantity of SNe Ia has contaminated interstellar space with Fe. Such a trend of chemical evolution is also implied by observations of stellar metallicity in the Milky Way, where $[\alpha/\text{Fe}]$ approaches the solar value as $[\text{Fe}/\text{H}]$ gets close to the solar abundance (e.g., Bensby et al. 2014; Hawkins et al. 2016; Nandakumar et al. 2025). Nonetheless, we will discuss the averaged properties of SNe integrated over time in Section 4.2.

Regarding only the X/Fe values, it is worth stressing that the solar abundance ratio is also observed in metal-richer systems (e.g., Centaurus, Fukushima et al. 2022; Mernier et al. 2025). In this sense, Mernier et al. (2018b) and Fukushima et al. (2023) performed systematic analyses and reported a ubiquitous solar chemical composition of the X-ray-emitting haloes in relatively hot systems. Our abundance pattern will be added as an additional example to support this picture. Importantly, previous systematic studies have suffered from large uncertainties in abundance measurement (20–40%), including differences among samples, in exchange for long integrated exposures (4.5 Ms, Mernier et al. 2018b; 0.8 Ms, Fukushima et al. 2023). The limited energy resolu-

Table 2. Summary of the theoretical SN yield predictions tested in this work.

label	SN type	description	reference
W7	massive Ia	1D simulation, pure deflagration	Leung & Nomoto (2018)
LN18p	massive Ia	2D simulation, pure deflagration	Leung & Nomoto (2018)
LN18-Lp	massive Ia	2D simulation, pure deflagration, low core density	Leung & Nomoto (2018)
LN18-Hp	massive Ia	2D simulation, pure deflagration, high core density	Leung & Nomoto (2018)
F14	massive Ia	3D simulation, pure deflagration	Fink et al. (2014)
F14-L	massive Ia	3D simulation, pure deflagration, low core density	Fink et al. (2014)
F14-H	massive Ia	3D simulation, pure deflagration, high core density	Fink et al. (2014)
WDD2	massive Ia	1D simulation, delayed detonation	Leung & Nomoto (2018)
LN18	massive Ia	2D simulation, delayed detonation	Leung & Nomoto (2018)
LN18-L	massive Ia	2D simulation, delayed detonation, low core density	Leung & Nomoto (2018)
LN18-H	massive Ia	2D simulation, delayed detonation, high core density	Leung & Nomoto (2018)
S13	massive Ia	3D simulation, delayed detonation	Seitenzahl et al. (2013)
S13-L	massive Ia	3D simulation, delayed detonation, low core density	Seitenzahl et al. (2013)
S13-H	massive Ia	3D simulation, delayed detonation, high core density	Seitenzahl et al. (2013)
Pak12	light Ia	double degenerate, violent merger	Pakmor et al. (2012)
Sh18	light Ia	double degenerate, double detonation	Shen et al. (2018)
LN20	light Ia	single degenerate, double detonation	Leung & Nomoto (2020)
N13	CC	no rotation	Nomoto et al. (2013)
Suk16	CC	no rotation, neutrino transport included	Sukhbold et al. (2016)
LC18	CC	no rotation, massive stars $> 25M_{\odot}$ do not undergo SNe	Limongi & Chieffi (2018)

tion of CCD instruments and the poor reconstruction of dispersive spectra from extended sources, for instance, would also contribute to significant uncertainties. We demonstrated that the Resolve data enable us to estimate abundances with 10–20% accuracy among each metal, excluding Cr and Mn, with a single observation of only 217 ks. This fact suggests a decisive advantage in measuring the chemical abundance of the hot ICM, and will ensure the presence of XRISM in future spectroscopic observations of galaxy clusters.

4.2 Enrichment by SN explosions

We consider a linear combination of the calculations of SN nucleosynthesis to reproduce the observed abundance pattern from Si/Fe to Ni/Fe. We adopt calculated models for SN Ia of Seitenzahl et al. (2013), Fink et al. (2014), and Leung & Nomoto (2018) for SNe from a massive white dwarf (about $1.4M_{\odot}$) and Pakmor et al. (2012), Shen et al. (2018), and Leung & Nomoto (2020) for those of light progenitors (about $0.8M_{\odot}$). For CCSNe from various progenitor masses, three yields (Nomoto et al. 2013; Sukhbold et al. 2016; Limongi & Chieffi 2018) are adopted, each of which is averaged over a Salpeter initial mass function (Salpeter 1955). The models used in this work are summarised in table 2, and we fit the observed pattern with 126 SN combination models. When fitting the pattern and calculating fit statistics, modelling uncertainties are added in quadrature to statistical errors for each X/Fe value.

The best-fitting result given by the combination of the F14, Sh18, and Suk16 models is presented in figure 3(a), which yields a good fit with $\chi^2/\text{dof} = 1.1$. This combination model suggests that the number ratio of SN Ia to total SNe is about 23% (massive, 7%; light 16%) and SNe Ia produce 67% of Fe in the ICM. A previous study of ICM enrichment by SNe in Ophiuchus estimated the SN Ia fraction to be 10–20% at $\lesssim 100$ kpc (Gatuzz et al. 2023), which is comparable to our estimate. To reveal the census of SNe Ia predicted by current models, we also plot the contribution of SNe to Fe against SNe Ia/SNe for all combinations

(figure 3(b)). While considering various theoretical assumptions of each model (table 2), the better-fitting models ($\chi^2/\text{dof} < 2$) illustrate a similar enrichment scenario with a moderate fraction ($21 \pm 5\%$) of SNe Ia producing the bulk of Fe ($66 \pm 5\%$) in the ICM, where $52 \pm 23\%$ of them come from massive progenitors. Such a population of SNe Ia is globally consistent with previous studies of galaxy clusters (e.g., Sato et al. 2007; Simionescu et al. 2015; Ezer et al. 2017; Simionescu et al. 2019; Erdim et al. 2021).

Interestingly, some combinations provide a marginal fraction of SNe Ia below 10% despite large χ^2/dof values (lower left area in figure 3(b)), wherein the CCSN model is assumed to be LC18. In the LC18 model, Limongi & Chieffi (2018) assumes that massive stars $> 25M_{\odot}$ do not undergo an SN explosion and contribute to enrichment via the stellar mass-loss channel only. The lack of massive CCSNe leads to relatively low Ar/Fe and Ca/Fe ratios about 1 solar compared to other models, and mixing with SNe Ia worsens the fit, as these abundances are reduced to subsolar values. Unlike short-timescale systems subject to ongoing star formation activity, such as starburst galaxies (Arp 299, Mao et al. 2021; M82, Fukushima et al. 2024), the ICM of galaxy clusters with a long enrichment history may require a significant contribution from a massive stellar population.

4.3 Implications into the “Ca conundrum”

Figure 4(a) illustrates the graphical implications of how well recent models predict each X/Fe abundance ratio. At first glance, the Ca/Fe ratios are uniformly underestimated compared to the observed value, that is, to the solar composition. Such a *hypocalcemia* problem of nucleosynthesis models, known as the “Ca conundrum”, has been mentioned in many previous studies (e.g., de Plaa et al. 2007; Werner et al. 2008; Simionescu et al. 2019; Fukushima et al. 2022). One solution is proposed by Mulchaey et al. (2014) and Mernier et al. (2016), where the Ca enrichment of the ICM can be attributed not only to normal SNe Ia but also to Ca-rich gap transients (Filippenko et al. 2003; Perets et al. 2010;

Waldman et al. 2011). Both studies estimated that this subclass accounts for about 20–30% of total SN Ia events.

We also include the predicted yield of Ca-rich events (W11 from Waldman et al. 2011), and the combination model with LN18-Hp, Sh18, and Suk16 significantly improves the fit as shown in figure 4(b). In this model, we estimate the fraction of Ca-rich gap transients to total SNe Ia is 21%, where other good combinations ($\chi^2/\text{dof} < 2$) yield 13–33% fraction. Our estimation is consistent with the estimation by Mulchaey et al. (2014) and Mernier et al. (2016). While the fraction of galactic Ca-rich events had been estimated to be < 20% (e.g., Perets et al. 2010; Li et al. 2011), more updated observational constraints allow more frequent events > 30% at larger distances from galaxies (Frohmaier et al. 2018). Given that the abundance pattern of the ICM may be more consistent with those of the outer edge of galaxies than of their inner region, dominated by the member stellar population, Ca-rich transients can naturally solve the Ca conundrum.

5 Conclusions

We have analysed the Resolve data of the Ophiuchus cluster core and measured the metal abundance pattern. The results are summarised as follows.

1. We find that the abundance pattern of the Ophiuchus core is consistent with solar, which is reminiscent of the Hitomi constraint of Perseus (Simionescu et al. 2019). The uncertainties of abundance measurement are 10–20%, less than in previous systematic studies using large samples (e.g., Mernier et al. 2018b), demonstrating an excellent capability of XRISM for elemental abundance studies.
2. Recent SN nucleosynthesis models prefer a specific chemical enrichment history that constitutes 15–25% of total SNe being SN Ia, and 60–70% of Fe in the ICM being forged by them. The CCSN contribution from massive stars with $> 25M_\odot$ progenitors may be crucial to reproducing the observed abundances accurately, which differs from the case of starburst systems (e.g., Mao et al. 2021).
3. The observed Ca/Fe ratio about 1 solar is hard to explain by the standard SN combination model. The Ca-rich gap transients, thermonuclear events classified as a subclass of SNe Ia, can be one solution with a substantial contribution of about 13–33% of SNe Ia, which is in plausible agreement with the pictures provided by direct SN studies (e.g., Frohmaier et al. 2018).

Acknowledgments

The authors are grateful to the anonymous referee for their helpful comments and suggestions, improving our manuscript drastically. We appreciate Dr. Y. Kanemaru for providing excellent Xtend images. We also thank the project members who are working on the mission and science operations of XRISM. The Japan Aerospace Exploration Agency (JAXA), the National Aeronautics and Space Administration (NASA), and the European Space Agency (ESA) have collaborated to develop and operate XRISM internationally. In addition to the three space agencies, universities and research institutes from Japan, the United States, and European states have contributed to the development of satellites, science instruments, and data-processing software, as well as to the further preparation of scientific observation plans. This work is also based on XMM-Newton, the ESA science mission with instruments and contributions directly funded by ESA Member States and NASA of the

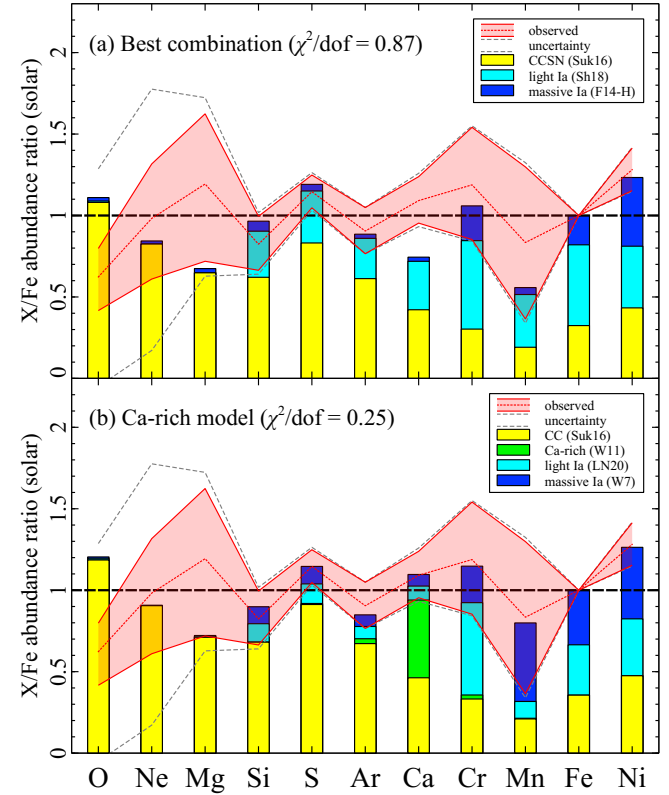


Fig. 5. (a) The same as figure 3(a), but including the O/Fe, Ne/Fe, and Mg/Fe ratios. (b) The same as figure 4(b) with the O/Fe, Ne/Fe, and Mg/Fe ratios.

United States. The figures in this article were generated using VEUSZ (<https://veusz.github.io/>) and PYTHON version 3.10.

Funding

This work was supported by JSPS KAKENHI grant Nos. 22H00158, 23H04899, and 25H00672 (YF).

Data availability

The XRISM data set analysed in this article is for exclusive use until April 16, 2026; afterwards, the data will be made available publicly via the XRISM data archive ⁵ ⁶. The XMM-Newton Science Archive⁷ stores and distributes the data set analysed in the Appendix section.

Appendix 1 O, Ne, and Mg abundances

In this Appendix, we present the O, Ne, and Mg abundances in our abundance pattern. We derive these abundances using the XMM-Newton archival data set (OBSID = 0505150101), pointing the centre of the Ophiuchus cluster. To compare with the Resolve results with a modest spatial resolution, we extract spectra from the 2.5 arcmin core from MOS (Turner et al. 2001) and pn (Strüder

⁵ <https://data.darts.isas.jaxa.jp/pub/xrism/data/obs/>

⁶ <https://heasarc.gsfc.nasa.gov/FTP/xrism/data/obs/>

⁷ <https://nxsa.esac.esa.int/nxsa-web/>

et al. 2001), covering the entire Resolve FoV and its surrounds. Similar to the analysis procedures described in Sections 3.1 and 3.2, we employ the 1T, 2T, and DEM models in both the 0.4–9 keV and 0.4–2 keV bands and estimate the O, Ne, Mg, and Fe abundances. The elements heavier than Al are linked to Fe, and the others follow the same setting in Section 3.1.

The Fe abundance is well constrained around 0.6–0.7 solar, and the O, Ne, and Mg ones show large differences of up to 50% between the broad and local band fits across all modelling. What causes this large discrepancy may simply be the limitations of the energy resolution of the CCD instruments and/or the relatively high temperature of the ICM ($kT \sim 8$ –9 keV), as well as possible different metal content of the low-temperature components responsible for these light metals from that of the high-temperature components accessible with the Resolve spectrum. Mernier et al. (2025) discusses such a plausible multi-metallicity ICM in Centaurus with a stronger cool core than that of Ophiuchus. Nevertheless, we adopt the results from the DEM model in the 0.4–2 keV band: O/Fe = 0.6 ± 0.2(±0.6) solar, Mg/Fe = 0.9 ± 0.4(±0.7) solar, and Ne/Fe = 1.2 ± 0.5(±0.6) solar.

Figures 5(a) and (b) demonstrate the abundance pattern (O/Fe, Ne/Fe, Mg/Fe, Si/Fe, S/Fe, Ar/Fe, Ca/Fe, Cr/Fe, Mn/Fe, and Ni/Fe) and the best-fitting SN combination models. With the light α -element abundances, despite large systematic errors, the preferred enrichment scenario of better combinations yields 9 ± 7% and 9 ± 5% for massive and light SNe Ia, respectively, and 82 ± 7% for CCSNe. As well, the Ca-rich transient contribution improves the fit with a fraction 24 ± 5% of SNe Ia. These results are completely consistent with the main conclusions in Sections 4.2 and 4.3. The crucial advantage of including the contribution from the Ca-rich transient channel is also discussed in Sarkar et al. (2025), focusing on the strong cool core cluster Abell 2029 with the XRISM data sets.

References

Arnaud K. A., 1996, in Jacoby G. H., Barnes J., eds, Astronomical Society of the Pacific Conference Series Vol. 101, Astronomical Data Analysis Software and Systems V. p. 17

Bensby T., Feltzing S., Oey M. S., 2014, *A&A*, **562**, A71

Cappelluti N., et al., 2017, *ApJ*, **837**, 19

Cash W., 1979, *ApJ*, **228**, 939

Durret F., Wakamatsu K., Nagayama T., Adami C., Biviano A., 2015, *A&A*, **583**, A124

Erdim M. K., Ezer C., Ünver O., Hazar F., Hudaverdi M., 2021, *MNRAS*, **508**, 3337

Ezer C., Bulbul E., Nihal Ercan E., Smith R. K., Bautz M. W., Loewenstein M., McDonald M., Miller E. D., 2017, *ApJ*, **836**, 110

Filippenko A. V., Chornock R., Swift B., Modjaz M., Simcoe R., Rauch M., 2003, IAU Circ., **8159**, 2

Fink M., et al., 2014, *MNRAS*, **438**, 1762

Frohmaier C., Sullivan M., Maguire K., Nugent P., 2018, *ApJ*, **858**, 50

Fujita Y., et al., 2008, *PASJ*, **60**, 1133

Fujita Y., Fukushima K., Sato K., Fukazawa Y., Kondo M., 2025, *PASJ*, **77**, S270

Fukushima K., Kobayashi S. B., Matsushita K., 2022, *MNRAS*, **514**, 4222

Fukushima K., Kobayashi S. B., Matsushita K., 2023, *ApJ*, **953**, 112

Fukushima K., Kobayashi S. B., Matsushita K., 2024, *A&A*, **686**, A96

Gastaldello F., Simionescu A., Mernier F., Biffi V., Gaspari M., Sato K., Matsushita K., 2021, *Universe*, **7**, 208

Gatuzz E., et al., 2023, *MNRAS*, **526**, 396

HI4PI Collaboration et al., 2016, *A&A*, **594**, A116

Hawkins K., Masseron T., Jofré P., Gilmore G., Elsworth Y., Hekker S., 2016, *A&A*, **594**, A43

Hitomi Collaboration et al., 2017, *Nature*, **551**, 478

Hitomi Collaboration et al., 2018, *PASJ*, **70**, 9

Ishisaki Y., et al., 2025, *Journal of Astronomical Telescopes, Instruments, and Systems*, **11**, 042023

Kaastra J. S., 2017, *A&A*, **605**, A51

Kaastra J. S., Mewe R., Nieuwenhuijzen H., 1996, in UV and X-ray Spectroscopy of Astrophysical and Laboratory Plasmas. pp 411–414

Kaastra J. S., Raassen A. J. J., de Plaa J., Gu L., 2025, SPEX X-ray spectral fitting package, doi:10.5281/zenodo.17313851, <https://doi.org/10.5281/zenodo.17313851>

Kelley R. L., et al., 2025, *Journal of Astronomical Telescopes, Instruments, and Systems*, **11**, 042026

Leung S.-C., Nomoto K., 2018, *ApJ*, **861**, 143

Leung S.-C., Nomoto K., 2020, *ApJ*, **888**, 80

Li W., et al., 2011, *MNRAS*, **412**, 1441

Limongi M., Chieffi A., 2018, *ApJS*, **237**, 13

Liu A., Zhai M., Tozzi P., 2019, *MNRAS*, **485**, 1651

Lodders K., Palme H., Gail H. P., 2009, Abundances of the Elements in the Solar System. Springer Berlin, Heidelberg, pp 560–598 (arXiv:0901.1149), doi:10.1007/978-3-540-88055-4_34

Mao J., et al., 2021, *ApJL*, **918**, L17

Mernier F., et al., 2016, *A&A*, **595**, A126

Mernier F., et al., 2018a, *Space Sci. Rev.*, **214**, 129

Mernier F., et al., 2018b, *MNRAS*, **480**, L95

Mernier F., et al., 2025, arXiv e-prints, p. arXiv:2512.11028

Million E. T., Allen S. W., Werner N., Taylor G. B., 2010, *MNRAS*, **405**, 1624

Mulchaej J. S., Kasliwal M. M., Kollmeier J. A., 2014, *ApJL*, **780**, L34

Nandakumar G., Ryde N., Schultheis M., Rich R. M., di Matteo P., Thorsbro B., Mace G., 2025, *ApJL*, **982**, L14

Noda H., et al., 2025, *PASJ*, **77**, S10

Nomoto K., Kobayashi C., Tominaga N., 2013, *ARA&A*, **51**, 457

Pakmor R., Kromer M., Taubenberger S., Sim S. A., Röpke F. K., Hillebrandt W., 2012, *ApJL*, **747**, L10

Perets H. B., et al., 2010, *Nature*, **465**, 322

Rose T., et al., 2025, *ApJ*, **990**, 42

Salpeter E. E., 1955, *ApJ*, **121**, 161

Sanders J. S., 2023, Clusters of Galaxies. Springer Nature Singapore, pp 173–207, doi:10.1007/978-981-99-4409-5_8

Sarkar A., et al., 2025, *ApJL*, **995**, L26

Sato K., Tokoi K., Matsushita K., Ishisaki Y., Yamasaki N. Y., Ishida M., Ohashi T., 2007, *ApJL*, **667**, L41

Seitenzahl I. R., Cescutti G., Röpke F. K., Ruiter A. J., Pakmor R., 2013, *A&A*, **559**, L5

Shen K. J., Kasen D., Miles B. J., Townsley D. M., 2018, *ApJ*, **854**, 52

Simionescu A., Werner N., Urban O., Allen S. W., Ichinohe Y., Zhuravleva I., 2015, *ApJL*, **811**, L25

Simionescu A., et al., 2019, *MNRAS*, **483**, 1701

Strüder L., et al., 2001, *A&A*, **365**, L18

Sukhbold T., Ertl T., Woosley S. E., Brown J. M., Janka H. T., 2016, *ApJ*, **821**, 38

Tashiro M., et al., 2025, *PASJ*, **77**, S1

Turner M. J. L., et al., 2001, *A&A*, **365**, L27

Uchida H., et al., 2025, *PASJ*, **77**, S23

Verner D. A., Ferland G. J., Korista K. T., Yakovlev D. G., 1996, *ApJ*, **465**, 487

Waldman R., Sauer D., Livne E., Perets H., Glasner A., Mazzali P., Truran J. W., Gal-Yam A., 2011, *ApJ*, **738**, 21

Werner N., Durret F., Ohashi T., Schindler S., Wiersma R. P. C., 2008, *Space Sci. Rev.*, **134**, 337

Werner N., et al., 2016, *MNRAS*, **460**, 2752

Willingale R., Starling R. L. C., Beardmore A. P., Tanvir N. R., O'Brien P. T., 2013, *MNRAS*, **431**, 394

XRISM Collaboration et al., 2024, *PASJ*, **76**, 1186

XRISM Collaboration et al., 2025a, *PASJ*, **77**, S242

XRISM Collaboration et al., 2025b, *Nature*, **638**, 365

XRISM Collaboration et al., 2025c, *ApJL*, **982**, L5

XRISM Collaboration et al., 2025d, *ApJL*, **985**, L20

de Plaa J., 2013, *Astronomische Nachrichten*, **334**, 416

de Plaa J., Werner N., Bleeker J. A. M., Vink J., Kaastra J. S., Méndez M., 2007, *A&A*, **465**, 345